

3-Dimensional Scanning of Entire Unit Cells in Single Nanoparticles

Junyoung Heo,^[a, b] Dohun Kang,^[a, b] Sungin Kim,^[a, b] Hoje Chun,^[c] Byungchan Han,^{*, [c]}
Byung Hyo Kim,^{*, [b, d]} and Jungwon Park^{*, [a, b, e, f]}

Abstract: Properties of nanomaterials such as optical, electrical, and chemical properties are strongly correlated with lattice symmetry, making characterization of lattice symmetry essential. We introduce a symmetry analysis method using 3D atomic coordinates obtained by Brownian one-particle 3D reconstruction. The method allows direct and quantitative analysis of symmetrical properties and delivers local structural

characteristics of individual platinum (Pt) nanoparticles in unit-cell level. Local structural deformations of the Pt nanoparticles such as lattice distortion and internal symmetry breakage are demonstrated, revealing that the crystal structure of sub-3 nm Pt nanoparticles generally maintains FCC crystallinity and exhibits localized deviation from their bulk counterpart.

Introduction

The lattice symmetry affects various physical properties of materials.¹ In classical crystallographic theory, lattice symmetry of bulk crystal is generally conserved in a long range. However, recent development of material analysis reveals that the symmetry can be readily broken, especially for nanomaterials, induced by the presence of surface ligands,^{2,3} high surface to volume ratio,^{4,5} and incorporation of dopants,^{6,7} thus nanomaterials can have distinctive properties for application.⁸ For example, photoluminescence of nanomaterials can be enhanced by symmetry breakage, through mixing of hole spins and their parity sublevels.⁹ Gold nanoparticle with symmetry breakage introduced by small defects shows unique optical properties.¹⁰ In addition, the symmetry breakage regulates the

interaction between nanomaterials by creating dipole moment, inducing self-assembly process.^{11,12} Mirror symmetry broken, or chiral, nanomaterials can polarization-selectively tune amplitude and phase of light¹³ and interact with chiral biomolecules.¹⁴ Thus, the intriguing properties originated from symmetry-breaking of nanoparticles highlight the need for the symmetry analysis of nanomaterials.

The unique structures of nanoparticles with deviation from perfect crystal have been investigated by variety of methods.^{15–19} For lattice symmetry, indirect methods such as x-ray or neutron total scattering, Raman spectroscopy, and FTIR spectroscopy^{20–23} have been used. The scattering-based analysis provides pair distribution function (PDF) that includes types and length of bonds between atoms. For example, temperature-dependent symmetry reduction and generation of dislocation in nanomaterial are studied by tracking peak addition and intensity difference of PDF.⁵ More recent studies show that PDF analysis enables quantitative description of melting transition, regardless of shape, size, chemical compositions, and surrounding environment.^{24,25} Symmetry information can also be extracted from the vibrational modes of bonding between atoms, mainly characterized by Raman and FT-IR spectroscopy.²³ However, those methods only provide averaged symmetry in a batch of materials. In addition, the analysis of experimentally obtained information to understand lattice symmetry in these indirect methods usually rely on modelling and fitting. The ideal method for the symmetry analysis of nanomaterials requires overcoming these limitations and enabling characterization of the local symmetry in unit cell level.

The 3D full atomic coordinates of individual nanoparticles in liquid phase can be obtained by a recently developed structure analysis method, 'Brownian one-particle reconstruction'.²⁶ Time-series atomic-resolution images of freely rotating nanoparticles are obtained by using liquid-phase transmission electron microscopy. Then, the series of images are reconstructed to 3D structure by assigning projection direction of each images. 3D atomic structures obtained from the Brownian one-particle reconstruction yield an opportunity to understand structures based on symmetry in a unit cell level, and their correlation with interactions with

[a] J. Heo, D. Kang, S. Kim, Prof. J. Park
School of Chemical and Biological Engineering
and Institute of Chemical Processes
Seoul National University
Seoul 08826 (Republic of Korea)
E-mail: jungwonpark@snu.ac.kr


[b] J. Heo, D. Kang, S. Kim, Prof. B. Hyo Kim, Prof. J. Park
Center for Nanoparticle Research
Institute for Basic Science (IBS)
Seoul 08826 (Republic of Korea)

[c] H. Chun, Prof. B. Han
Department of Chemical & Biomolecular Engineering
Yonsei University
Seoul 03722 (Republic of Korea)
E-mail: bchan@yonsei.ac.kr

[d] Prof. B. Hyo Kim
Department of Organic Materials and Fiber Engineering
Soongsil University
Seoul 06978 (Republic of Korea)
E-mail: byunghyokim@ssu.ac.kr

[e] Prof. J. Park
Institute of Engineering Research, College of Engineering
Seoul National University
Seoul 08826 (Republic of Korea)

[f] Prof. J. Park
Advanced Institutes of Convergence Technology
Seoul National University
Gyeonggi-do 16229 (Republic of Korea)

 Supporting information for this article is available on the WWW under <https://doi.org/10.1002/cnma.202200057>

surrounding solvent molecules, ligands, and other nanoparticles in realistic liquid environment.

Here, we introduce lattice symmetry analysis of unit cell structures of platinum (Pt) nanoparticles. From atomic coordinates derived from atomic resolution 3D reconstruction of platinum nanoparticle, 26 symmetries of entire single unit cells in nanoparticles are directly investigated. Observation of local structural deformation through symmetry analysis improves our understanding for structure of ligand protected platinum nanoparticles in liquid phase.

Results and Discussion

Bulk Pt unit cell has symmetric face centered cubic (FCC) structure, with $Fm\bar{3}m$ space group. The FCC structure with $Fm\bar{3}m$ space group, including bulk Pt unit cell structure, is completely symmetric for six types of symmetries: 4-fold rotational symmetry for $\langle 100 \rangle$, mirror symmetry for planes perpendicular to $\langle 100 \rangle$, 3-fold rotational symmetry for $\langle 111 \rangle$, 3-fold rotoinversion symmetry for $\langle 111 \rangle$, 2-fold rotational symmetry for $\langle 110 \rangle$, and mirror symmetry for planes perpendicular to $\langle 110 \rangle$.

The breakage of symmetry is quantified by continuous symmetry measure (CSM).^{1,27–29} CSM is generally defined as mean square displacement between a shape and its 'symmetrized' structure, which is defined as symmetric and closest shape from original. Detailed procedure for calculating the CSM values of each atom is described in Figure 1a, Method, and Figure S1. For each of six types of symmetries for FCC structure of Pt nanoparticles, the maximum of measured CSM values among the ones from different directions of the same symmetry type is presented in the Figure 1 since the breakage of the symmetry along at least one direction indicates the symmetry of the unit cell is broken. For example, the presented CSM value for 4-fold rotational symmetry for $\langle 100 \rangle$ is the maximum value among the measured CSM values of 4-fold rotational symmetries for [100], [010], and [001].

The correlation between atomic deformation and CSM value changes are simulated by using a model unit cell, as shown in Figure 1b. We build the deformed unit cell structure by moving a single atom through [100] direction and define the 'atomic deformation' as the distance (Å) between the moved single atom and its original position. Deviation of the atomic coordinate from the ideal structure leads to increase of CSM values. Mirror symmetries for $\langle 100 \rangle$ and $\langle 110 \rangle$ have lower CSM values than other types of symmetries, because of difference of calculation method. We apply the CSM calculation method to model ~3 nm sized nanoparticles with ideal FCC, monoclinic, and icosahedron structures to test applicability of the method to synthesized nanocrystals (see Figure S2). CSM studies of the modelled FCC nanocrystals show all type of symmetry preserved. The high CSM values of atoms that locate far from the center are from the symmetry breakage of surface atoms. In the case of monoclinic nanoparticles, 2-fold symmetries and one of 4-fold rotational symmetry are preserved, while other types of symmetries including 4-fold and 3-fold symme-

tries show high CSM values. On the other hand, icosahedron nanoparticle, that has absence of long-range of symmetry due to grain boundaries, shows fluctuating CSM values along with atomic positions. The model studies indicate that the CSM value is a useful descriptor that can be applied to the symmetry analysis based on 3D atomic coordinates of nanoparticles.

The symmetry analysis is applied to the realistic 3D atomic coordinate structures of Pt nanoparticles obtained by liquid phase TEM. Pt nanoparticles are 2–3 nanometers in size, surrounded by polyvinylpyrrolidone (PVP) ligands, and are at room temperature. Representative unit cell structures and their corresponding CSM values of a Pt nanoparticles are displayed in Figure 1c, revealing the correlation between the increase of CSM value and the degree of deformation of unit cell structure. Note that the absence of the adjacent atoms causes complete symmetry breakage, making CSM values of surface atoms and defect sites very high (see fourth column of Figure 1c). CSM values for 3-fold rotoinversion symmetry are exemplarily presented because 3-fold rotoinversion symmetry for $\langle 111 \rangle$ is related to distinct ABC stacking of FCC structure (Figure 1d). While unit cell structures with small CSM values are almost symmetric at $\langle 100 \rangle$, $\langle 110 \rangle$, and $\langle 111 \rangle$ direction, the unit cell structures with large CSM values remarkably deviate from the symmetric structure. Surface atoms, which are apart from the core of the Pt nanoparticle where lattice symmetry of unit cell is well preserved, show significantly large CSM values compared to the core atoms as shown in the color map in Figure 1d and the fourth row of Figure S3.

We analyze six types of symmetries to understand details of lattice deformation in a single unit cell level. For all six types of symmetries, CSM values drastically increase at near the surface as shown in Figure 1e. This tendency originates from the marginal disorders of crystal structures of the Pt nanoparticle that occur near the surface, that are consistent with deviations of interatomic distances near the surface shown in the previous study.²⁶ CSM values of mirror symmetries are in general lower than the others because of the difference in calculation method. This trend is also consistently observed in randomly deformed atomic coordinates (see Figure S4).

Correlations between different types of symmetries are investigated to understand how the lattice structures are deformed. 3-fold rotoinversion symmetry for $\langle 111 \rangle$, 4-fold rotational symmetry for $\langle 100 \rangle$, 3-fold rotation symmetry for $\langle 111 \rangle$, and 2-fold rotational symmetry for $\langle 110 \rangle$ show high correlations between each other, as shown in Figure 1f and Table S1. Such correlations between CSM values for different types of symmetries indicate that deformations of the unit cell structure do not have any specific direction. Density functional theory (DFT) calculations also show that the symmetry deformation shows no preferential direction (see Methods and Figure S5). We calculate the energy difference for four model systems that contains deformation in certain symmetry direction while preserving others. The model structures are relaxed by fixing the overall volume and the boundary atom coordinates to account for the surface effects induced by ligands and solvent. The standard deviation of the energies for the four model systems with frozen configuration is $107 \text{ meV atom}^{-1}$,

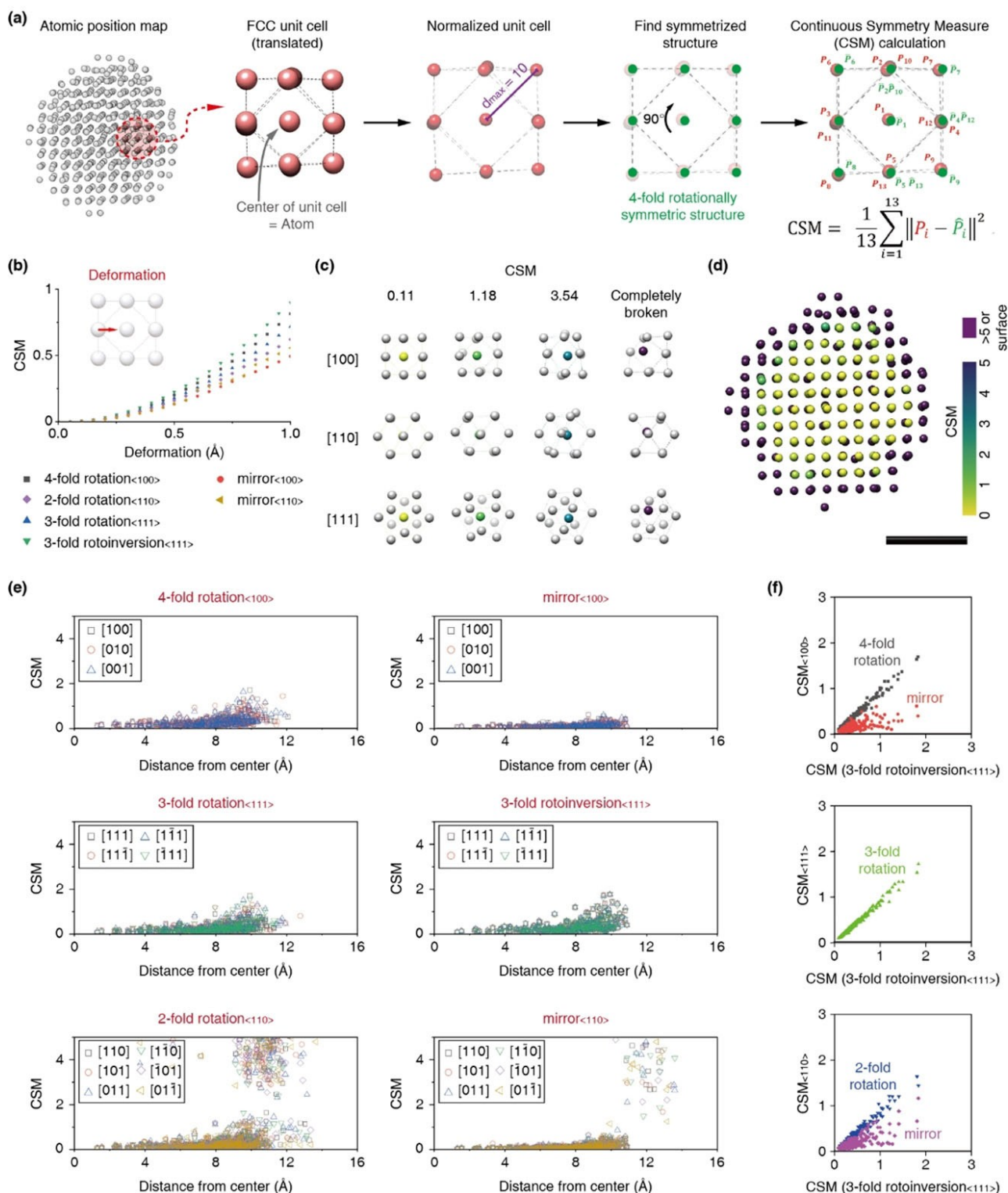


Figure 1. Quantitative symmetry analysis from 3D atomic structures. (a) Scheme for symmetry distance (CSM) calculation from an atomic position map. (b) Plots between deformation from perfect FCC and CSM for six types of symmetries. (c) Representative unit cell structures with different CSM values and (d) sliced symmetry map of a nanoparticle reconstructed via Brownian one particle reconstruction (Particle 4 in Ref. 26) colored with CSM value for 3-fold rotoinversion symmetry for <111>. Surface atoms can show unusually high CSM values with the absence of adjacent atoms. (e) Plots between CSM values for six different types of symmetries and radial distance of each atom from the center of mass. (f) Correlations between types of symmetries. Scale bar, 1 nm.

whereas the deviation is reduced to 43 meVatom⁻¹ once the structures are allowed to relax. The calculation results indicate

that structures, in which several types of symmetries are simultaneously broken, are more stable than structures with

symmetry breakage in a certain symmetry. Correlation plots from deformations with specific directions tend to differ from those observed in our result (see Figure S6). For example, if the unit cell structure transformed to tetragonal structure along uniaxial direction, three mirror symmetries for [100], [010], and [001] would be completely preserved.

We perform the same symmetry analysis to the previously reported atomic coordinate structures of six single-crystalline Pt nanoparticles.²⁶ Symmetry maps displayed at Figure 2a and Figure S3 show that six particles have different range of CSM values, showing that there is structural heterogeneity. CSM values in each nanoparticle are displayed in Figure 2b and Figure S7. In particle 1, very low CSM values are maintained throughout the particle. In most of particles, CSM values are generally high and increase toward the surface. The high CSM values can be explained by the unit cell distortion at near the surface and low coordination number of surface atoms less than 12. We obtain CSM values of atoms with coordination number 12 to rule out the effect of bond breakage of surface on symmetry reduction (see Figure S8). Unit cell structure distortion at near the surface is observed in most of the particles.

In some particles, notable increment of CSM values is also observed at the core of the particles. We analyzed internal structure and CSM value distribution of the particle 2, 3, and 6, that show high average CSM values (see Figure S9) and many outliers in their internal structure. A significant number of

internal atoms have high CSM value more than 5 (see Figure S10), and we define those atomic points as internal symmetry breakage points. In the internal symmetry breakage points, almost all types of symmetries are broken. The unit cell structures of internal symmetry breakage point are highly distorted from perfect FCC (see Figure 2c).

As Pt nanoparticles we study here have slight expansion of the averaged lattice parameters from their bulk counterparts,²⁶ we investigated the correlation between the unit cell symmetry and the lattice expansion. Particles with more expanded lattice parameter show larger CSMs, as shown in Figure 3a. Lattice expansion exerts stress to atoms, presumably leading to unit cell symmetry breakage. This observation is consistent with a previous report which confirmed that applying strain increases the density of dislocations in small nanomaterial.³⁰ Local lattice distortion can be attributed to interactions between nanoparticle surface and environment.³¹ Interactions with surface ligand and solvent molecules can induce unit cell structure distortion which is associated with lattice expansion. If nanomaterial is highly strained by surface interaction between nanoparticles and surroundings, internal structure of nanoparticles can be also affected, not only surface structure.^{3,31–35} In Pt nanoparticles with a size range of 2 to 3 nm which show structural heterogeneity, correlation between particle size and CSM values is not noticeable (Figure 3b).

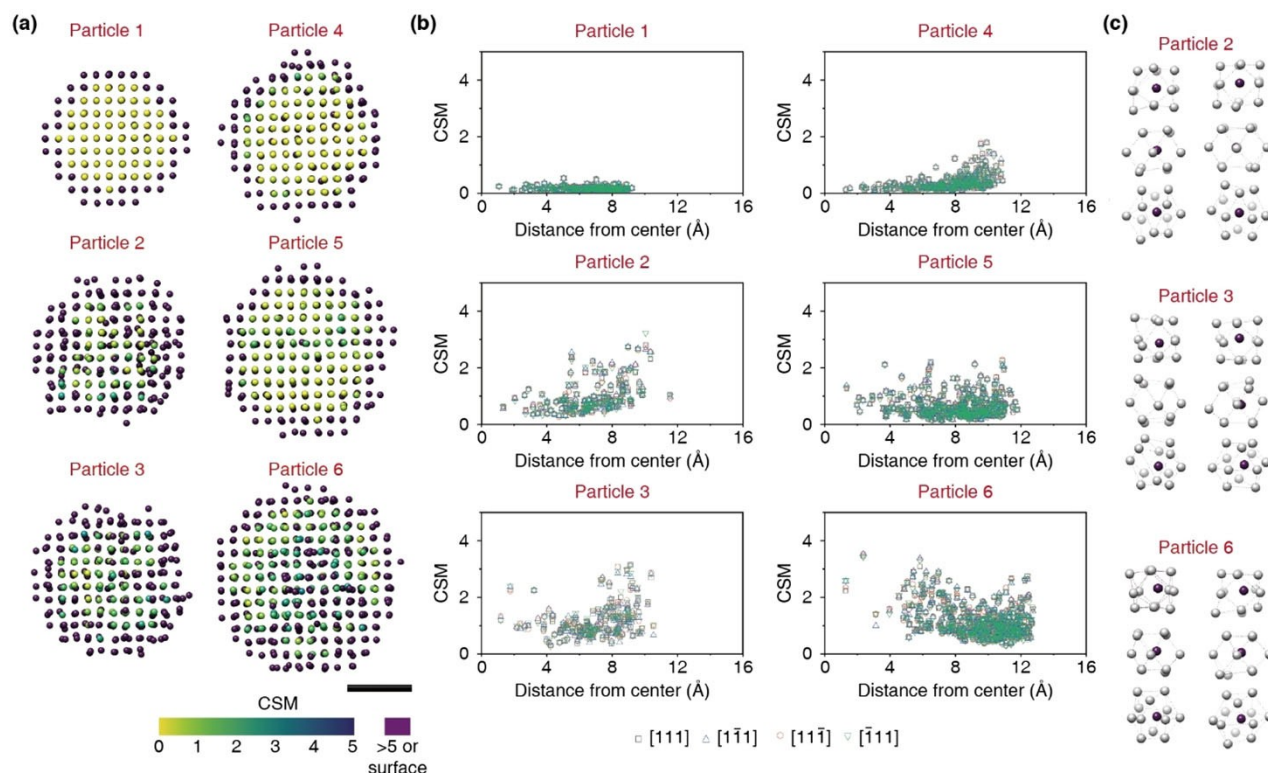


Figure 2. Symmetry analysis results from six particles. (a) Symmetry maps of six platinum nanoparticles reconstructed via Brownian one particle reconstruction, colored with CSM value for 3-fold rotoinversion symmetry for $\langle 111 \rangle$ direction. (b) Plots between CSM values (3-fold rotoinversion symmetry for $\langle 111 \rangle$) for six nanoparticles and radial distance of each atom from the center of mass. (c) Representative unit cell structures of internal symmetry breakage points in Particle 2, 3, and 6. Scale bar, 1 nm.

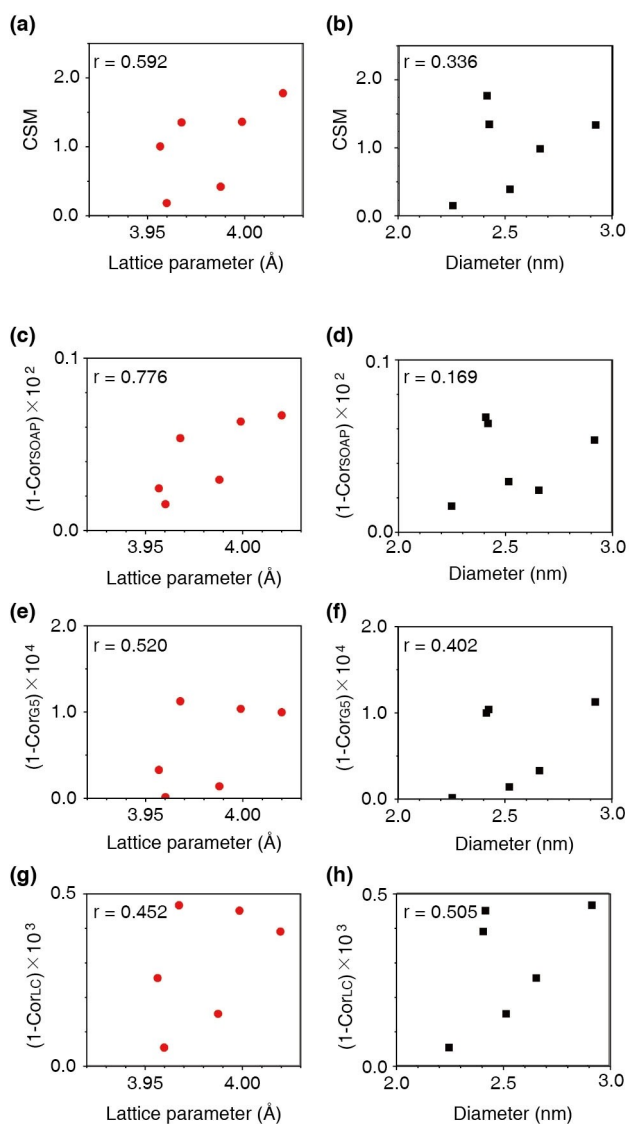


Figure 3. Relationship between symmetry breakage and particle properties. (a) Correlation between averaged lattice parameter and averaged CSM value (3-fold rotoinversion for $\langle 111 \rangle$) of each nanoparticle. (b) Correlation between nanoparticle diameter and averaged CSM value (3-fold rotoinversion for $\langle 111 \rangle$). (c, d) Correlation between averaged correlation value compared to ideal structure by using SOAP and particle properties. (e, f) Correlation between averaged correlation value compared to ideal structure by using G_5 symmetry function and particle properties. (g, h) Correlation between averaged correlation value compared to ideal structure by using local correlation-based spectra and particle properties.

We compare CSM with commonly used structural descriptors used for describing structural information such as smooth overlapping atomic density (SOAP),^{36,37} symmetry functions,³⁸ and local correlation-based spectrum.³⁹ While CSM is an efficient descriptor to investigate quantitative relationship between symmetry and the various material properties, other descriptors, mentioned above, are specifically important in atomization energy prediction or input for machine learning. CSM and the descriptors are applied to atom coordinate data of Pt individual obtained from Brownian one-particle reconstruction. To describe structural

deformation using SOAP spectra, vectors from symmetry functions, and local correlation-based spectra, correlations with bulk platinum FCC structure (Cor_{SOAP} , Cor_{G_5} , and Cor_{LC}) are calculated. The strong correlation between CSM and other descriptors confirms that CSM measured in a unit cell level is one of the useful descriptors to study crystal structure of nanocrystals (see Figure S11). Relationships between lattice expansion or particle size and other structural descriptors are also investigated, showing the similar relationships (Figure 3c–h).

Conclusion

In summary, lattice symmetries of 2–3 nm-sized Pt nanoparticles in liquid phase are investigated based on 3D atomic structure obtained from the Brownian one-particle reconstruction. Symmetry analysis reveals that unit cells at core are symmetric, but unit cell structures become disordered at near the surface. All types of symmetries are synchronously broken, indicating there is no specific direction in structural disorder. Some particles have internal symmetry breakage points. The lattice expansion induced by surface interactions affects lattice symmetry of Pt nanoparticles, both at surfaces and internal domains. The combination of reconstruction and symmetry analysis provides direct information that elucidates local unit cell symmetry. The relationship between size and symmetry breakage in wider range of particle sizes is an important topic for future study, which will potentially elucidate the size regime where structural characteristics are dependent on nanoscale-specific scaling laws. Such study can be carried out with the development of 3D structure analysis methods.

Methods

Continuous symmetry measure (CSM) calculation for single unit cell. Conventional FCC unit cell consists of 14 atoms (8 in tips and 6 in the face center). In this study, we translate the conventional FCC unit cell to place one atom at the center of unit cell; translated unit cell consists of 13 atoms (1 in body center and 12 nearest neighbor atoms).

CSM is defined as mean square displacement between a shape and its closest shape with symmetry preserved ('symmetrized' structure). The equation for CSM value calculation is as follows,

$$CSM = \frac{1}{N} \sum_{i=1}^N \|P_i - \hat{P}_i\| \quad (1)$$

where N is the number of atoms, P_i is the position of i th atom, and \hat{P}_i is the position of i th atom from the symmetrized structure. For the calculation, a single unit cell is designated by cropping one atom and its nearest neighbors from the 3D atomic structure, which have interatomic distances less than 3.5 Å. Normalization of the unit cell size is conducted by scaling the maximum distance among the distances between center atom of unit cell and its nearest neighbors as 10. Then, the normalized unit cell structure is symmetrized (detailed procedure of symmetrizing is depicted in Figure S1) and CSM is calculated between normalized unit cell and its symmetrized structure.

Computational Details of DFT calculations. First principles density functional theory (DFT) calculations were conducted through Vienna ab-initio simulation package (VASP).^{40,41} Perdew-Burke Ernzerhof (PBE)^{42,43} generalized gradient approximation (GGA) exchange-correlation functional and the projector-augmented wave (PAW) pseudopotentials^{44,45} were applied. The plane-wave basis set cutoff energy was 400 eV, and energy and forces convergence were 10^{-6} eV and 0.02 eV/Å, respectively. All calculations were spin polarized and a Monkhorst-Pack $4 \times 4 \times 4$ k-point mesh was used for $3 \times 3 \times 3$ Pt supercell. To investigate the correlation of the symmetry deformation direction, we utilized two different energies referenced to the optimized ideal structure. One is the energy from a single point calculation for the symmetry broken system in a certain direction, and the other is the energy of a relaxed structured while the volume and the boundary atoms are fixed during the geometry optimization. We captured the symmetry broken atoms of a unit cell inside the nanoparticle to correlate with thermodynamic stability. Zero-point energy (ZPE) was obtained by calculating all vibration modes of a supercell. The energy difference (ΔE) was calculated as equation (2), where E , E_{eq} and N mean total energy of model system and of bulk Pt, and number of atoms, respectively.

$$\Delta E = \frac{1}{N}(E - E_{eq}) \quad (2)$$

Calculation of other structural descriptors. SOAP is a structural descriptor describing local environment, with representing local density of atoms as a sum of Gaussian functions centered on neighbor atoms and central atom itself.^{36,37} The equation for calculation of SOAP spectrum at a certain position x is as follows,

$$\mathbf{P} = P_{n\nu}^{\mu\nu}(\mathbf{x}) = \sum_m c_{nlm}^{\mu}(\mathbf{x}) c_{n\nu m}^{\nu}(\mathbf{x}) \quad (3)$$

$$c_{nlm}^{\mu} = \int dV g_{nl}^{(\mu)}(r) \rho_N^{\mu}(r) Y_{lm}(\theta, \phi) \quad (4)$$

where μ and ν are types of atoms, N is the number of atoms, $g_{nl}^{(\mu)}(r)$ are radial basis functions, $Y_{lm}(\theta, \phi)$ are the spherical harmonics, and $\rho_N^{\mu}(r)$ are atomic density calculated by equation (5).

$$\rho_N^{\mu}(r) = \sum_{i=1}^N e^{-(r-P_i)^2} \quad (5)$$

where P_i is the position of i th point. The SOAPLite program is utilized for calculation of SOAP spectra with setting nMax as 3, Lmax as 3, and rCut as 5.^{36,37,46}

Radial symmetry functions, G_1 , G_2 , and G_3 , and angular symmetry functions, G_4 and G_5 , are used for describing 3D atomic structures.³⁸ They are defined as

$$G_{1,j} = \sum_j f_c(R_{ij}) \quad (6)$$

$$G_{2,j} = \sum_j e^{-\eta(R_{ij}-R_s)^2} \cdot f_c(R_{ij}) \quad (7)$$

$$G_{3,j} = \sum_j \cos(\kappa R_{ij}) \cdot f_c(R_{ij}) \quad (8)$$

$$G_{4,i} = 2^{1-\zeta} \sum_{j,k \neq i}^{all} (1 + \lambda \cos \theta_{ijk})^{\zeta} \cdot e^{-\eta(R_{ij}^2 + R_{ik}^2 + R_{jk}^2)} \cdot f_c(R_{ij}) \cdot f_c(R_{ik}) \cdot f_c(R_{jk}) \quad (9)$$

$$G_{5,i} = 2^{1-\zeta} \sum_{j,k \neq i}^{all} (1 + \lambda \cos \theta_{ijk})^{\zeta} \cdot e^{-\eta(R_{ij}^2 + R_{ik}^2)} \cdot f_c(R_{ij}) \cdot f_c(R_{ik}) \quad (10)$$

where $G_{k,i}$ are G_k symmetry functions for i th atom, R_{ij} is the distance between i th atom and j th atom, and $f_c(R_{ij})$ is the cutoff function depicted at equation (11),

$$f_c(R_{ij}) = \begin{cases} 0.5 \cdot \left[1 + \cos\left(\frac{\pi R_{ij}}{R_c}\right) \right] & (\text{for } R_{ij} \leq R_c) \\ 0 & (\text{for } R_{ij} > R_c) \end{cases} \quad (11)$$

where R_c is the cutoff radius, set as 5 Å. Symmetry functions have hyperparameters to tune, which are η and R_s for G_2 , κ for G_3 , and ζ , η , and λ for G_4 and G_5 . Vectors for G_2 , G_3 , G_4 , and G_5 consist of calculation results with different hyperparameters (hyperparameters for each element at vectors are summarized at Table S2). Vector with G_5 functions are used for comparing atomic environments with bulk platinum FCC.

Local correlation-based spectrum can be calculated from two-body correlations ($\mathbf{u}^{(1)}$ and $\mathbf{u}^{(2)}$ vector), three-body correlations ($\mathbf{u}^{(3)}$) and $\mathbf{u}^{(32)}$ vector), and higher order correlations.³⁹ Vector $\mathbf{u}^{(1)}$ is defined as

$$\mathbf{u}^{(1)} = \left[\rho_{i_1}^{(2)}(\sqrt{2}\sigma) \rho_{i_2}^{(2)}(\sqrt{2}\sigma) \rho_{i_3}^{(2)}(\sqrt{2}\sigma) \cdots \rho_{i_{(N_A-1)}}^{(2)}(\sqrt{2}\sigma) \right], \quad (12)$$

where $\rho_{i_1}^{(2)}$ is the overlap function depicted at equation (13),

$$\rho_{ij}^{(2)}(\sqrt{2}\sigma) = e^{-\frac{|r_i - r_j|^2}{4\sigma^2}} \quad (13)$$

where σ determines the spread of the Gaussian, set as 3 Å. Vector $\mathbf{u}^{(2)}$ is the set of eigenvalues of the matrix $\mathbf{K}^{(2)}$ with entries $K_{jk}^{(2)}$, which is described at equation (14).

$$K_{jk}^{(2)} = (1 - \delta_{jk}) \cdot \rho_{jk}^{(2)}(\sqrt{2}\sigma) \quad (j, k \neq i) \quad (14)$$

$$\delta_{jk} = \begin{cases} 1 & (\text{for } j = k) \\ 0 & (\text{for } j \neq k) \end{cases} \quad (15)$$

In this paper, $\mathbf{u}^{(1)}$ spectra from two-body correlation is used for comparing atomic environments with bulk platinum FCC.

To compare calculated SOAP spectra, vectors from symmetry functions, and local correlation-based spectra with those from bulk platinum FCC structure, correlation is calculated by using equation (16).

$$\text{Cor}_{<type>} = \frac{\mathbf{V}_{real} \cdot \mathbf{V}_{bulk}}{\sqrt{\|\mathbf{V}_{real}\| \cdot \|\mathbf{V}_{bulk}\|}} \quad (16)$$

where $\text{Cor}_{<type>}$ is correlation value from different type of descriptor vector ($<type> = \text{SOAP}, G_5, \text{ or } \text{LC}$), \mathbf{V}_{real} is descriptor vector from realistic atomic coordinates obtained by 3D reconstruction, and

V_{ideal} is descriptor vector from atomic coordinates from platinum bulk FCC structure.

Acknowledgements

J.P. acknowledges Institutes for Basic Science (IBS–R006-D1), the National Research Foundation of Korea (NRF) grant funded by the Korea government (MSIT) (No. NRF-2020R1A2C2101871, No. NRF-2017R1A5A1015365, and No. NRF-2019M3E6A1064877j). B.H.K., J.H., S.K., and J.P. acknowledge support by Samsung Science and Technology Foundation under project number SSTF-BA1802-08 for the development of the structural analysis algorithm. Theoretical computation was supported by the National Supercomputing Center with supercomputing resources including technical support (KSC-2019-CRE-0119). J.P. acknowledges support by Samsung Research Funding & Incubation Center of Samsung Electronics under Project Number SRFC-MA2002-03 for the use of computation resources. H.C. and B.H. were supported by the Global Frontier Program through the Global Frontier Hybrid Interface Materials (GFHIM) of the NRF funded by the Ministry of Science and ICT (project no. 2013M3A6B1078882). B.H.K. acknowledges the National Research Foundation of Korea (NRF) grant funded by the Korea government (No. NRF-2021R1C1C1014339).

Conflict of Interest

The authors declare no conflict of interest.

Data Availability Statement

The data that support the findings of this study are available from the corresponding author upon reasonable request.

Keywords: Symmetry analysis · Atomic structures · Nanoparticles · Unit-cell analysis · Structure-activity relationships

- [1] E. Estrada, D. Avnir, *J. Am. Chem. Soc.* **2003**, *125*, 4368–4375.
- [2] N. C. Anderson, M. P. Hendricks, J. J. Choi, J. S. Owen, *J. Am. Chem. Soc.* **2013**, *135*, 18536–18548.
- [3] F. Bertolotti, D. N. Dirin, M. Ibáñez, F. Krumeich, A. Cervellino, R. Frison, O. Voznyy, E. H. Sargent, M. V. Kovalenko, A. Guagliardi, N. Masciocchi, *Nat. Mater.* **2016**, *15*, 987–994.
- [4] S. Kastbjerg, N. Bindzus, M. Søndergaard, S. Johnsen, N. Lock, M. Christensen, M. Takata, M. A. Spackman, B. Brummerstedt Iversen, *Adv. Funct. Mater.* **2013**, *23*, 5477–5483.
- [5] Q. Zhao, A. Hazarika, L. T. Schelhas, J. Liu, E. A. Gauding, G. Li, M. Zhang, M. F. Toney, P. C. Sercel, J. M. Luther, *ACS Energy Lett.* **2020**, *5*, 238–247.
- [6] X. Tian, D. S. Kim, S. Yang, C. J. Ciccarino, Y. Gong, Y. Yang, Y. Yang, B. Duschatko, Y. Yuan, P. M. Ajayan, J. C. Idrobo, P. Narang, J. Miao, *Nat. Mater.* **2020**, *19*, 867–873.
- [7] M. Coduri, S. Checchia, M. Longhi, D. Ceresoli, M. Scavini, *Front. Chem.* **2018**, *6*, 526.
- [8] R. Chattot, O. Le Bacq, V. Beermann, S. Kühn, J. Herranz, S. Henning, L. Kühn, T. Asset, L. Guétaz, G. Renou, J. Drnec, P. Bordet, A. Pasturel, A. Eychmüller, T. J. Schmidt, P. Strasser, L. Dubau, F. Maillard, *Nat. Mater.* **2018**, *17*, 827–833.
- [9] P. C. Sercel, A. Shabaev, A. L. Efron, *Nano Lett.* **2017**, *17*, 4820–4830.
- [10] B. K. Canfield, S. Kujala, K. Laiho, K. Jefimovs, T. Vallius, J. Turunen, M. Kauranen, *J. Nonlinear Opt. Phys. Mater.* **2006**, *15*, 43–53.
- [11] E. S. Božin, C. D. Malliakas, P. Souvatzis, T. Proffen, N. A. Spaldin, M. G. Kanatzidis, S. J. L. Billinge, *Science* **2010**, *330*, 1660–1663.
- [12] Y. Wang, X. Peng, A. Abelson, P. Xiao, C. Qian, L. Yu, C. Ophus, P. Ercius, L.-W. Wang, M. Law, H. Zheng, *Sci. Adv.* **2019**, *5*, eaaw5623.
- [13] W. Li, Z. J. Coppens, L. V. Besteiro, W. Wang, A. O. Govorov, J. Valentine, *Nat. Commun.* **2015**, *6*, 8379.
- [14] T. Greber, Ž. Šljivčanin, R. Schillinger, J. Wider, B. Hammer, *Phys. Rev. Lett.* **2006**, *96*, 56103.
- [15] A. S. Barnard, L. A. Curtiss, *Nano Lett.* **2005**, *5*, 1261–1266.
- [16] B. Zandkarimi, A. N. Alexandrova, *J. Phys. Chem. Lett.* **2019**, *10*, 460–467.
- [17] D. M. Foster, Th. Pavloudis, J. Kioseoglou, R. E. Palmer, *Nat. Commun.* **2019**, *10*, 2583.
- [18] T. Ellaby, A. Varambhia, X. Luo, L. Briquet, M. Sarwar, D. Ozkaya, D. Thompsett, P. D. Nellist, C.-K. Skylaris, *Phys. Chem. Chem. Phys.* **2020**, *22*, 24784–24795.
- [19] Y. Yang, C.-C. Chen, M. C. Scott, C. Ophus, R. Xu, A. Pryor, L. Wu, F. Sun, W. Theis, J. Zhou, M. Eisenbach, P. R. C. Kent, R. F. Sabirianov, H. Zeng, P. Ercius, J. Miao, *Nature* **2017**, *542*, 75.
- [20] C. Castillo-Blas, J. M. Moreno, I. Romero-Muñoz, A. E. Platero-Prats, *Nanoscale* **2020**, *12*, 15577–15587.
- [21] T. L. Christiansen, S. R. Cooper, K. M. Ø. Jensen, *Nanoscale Adv.* **2020**, *2*, 2234–2254.
- [22] F. Bertolotti, L. Protesescu, M. V. Kovalenko, S. Yakunin, A. Cervellino, S. J. L. Billinge, M. W. Terban, J. S. Pedersen, N. Masciocchi, A. Guagliardi, *ACS Nano* **2017**, *11*, 3819–3831.
- [23] S. Roy, A. G. Joshi, S. Chatterjee, A. K. Ghosh, *Nanoscale* **2018**, *10*, 10664–10682.
- [24] L. Delgado-Callico, K. Rossi, R. Pinto-Miles, P. Salzbrenner, F. Baletto, *Nanoscale* **2021**, *13*, 1172–1180.
- [25] A. Van Teijlingen, S. A. Davis, S. R. Hall, *Nanoscale Adv.* **2020**, *2*, 2347–2351.
- [26] B. H. Kim, J. Heo, S. Kim, C. F. Reboul, H. Chun, D. Kang, H. Bae, H. Hyun, J. Lim, H. Lee, B. Han, T. Hyeon, A. Paul Alivisatos, P. Ercius, H. Emlund, J. Park, *Science* **2020**, *368*, 60–67.
- [27] H. Zabrodsky, S. Peleg, D. Avnir, *J. Am. Chem. Soc.* **1992**, *114*, 7843–7851.
- [28] C. Dryzun, *J. Comput. Chem.* **2014**, *35*, 748–755.
- [29] A. Steinberg, M. Karni, D. Avnir, *Chem. Eur. J.* **2006**, *12*, 8534–8538.
- [30] L. Wang, J. Teng, X. Sha, J. Zou, Z. Zhang, X. Han, *Nano Lett.* **2017**, *17*, 4733–4739.
- [31] T. Daio, A. Staykov, L. Guo, J. Liu, M. Tanaka, S. Matthew Lyth, K. Sasaki, *Sci. Rep.* **2015**, *5*, 13126.
- [32] B. Gilbert, H. Zhang, F. Huang, J. F. Banfield, Y. Ren, D. Haskel, J. C. Lang, G. Srajer, A. Jürgensen, G. A. Waychunas, *J. Chem. Phys.* **2004**, *120*, 11785–11795.
- [33] S. W. Im, H.-Y. Ahn, R. M. Kim, N. H. Cho, H. Kim, Y.-C. Lim, H.-E. Lee, K. T. Nam, *Adv. Mater.* **2020**, *32*, 1905758.
- [34] M. Epifani, E. Pellicer, J. Arbiol, N. Sergent, T. Pagnier, J. R. Morante, *Langmuir* **2008**, *24*, 11182–11188.
- [35] P. Strasser, S. Koh, T. Anniyev, J. Greeley, K. More, C. Yu, Z. Liu, S. Kaya, D. Nordlund, H. Ogasawara, M. F. Toney, A. Nilsson, *Nat. Chem.* **2010**, *2*, 454.
- [36] S. De, A. P. Bartók, G. Csányi, M. Ceriotti, *Phys. Chem. Chem. Phys.* **2016**, *18*, 13754–13769.
- [37] A. P. Bartók, R. Kondor, G. Csányi, *Phys. Rev. B* **2013**, *87*, 184115.
- [38] J. Behler, *J. Chem. Phys.* **2011**, *134*, 74106.
- [39] A. Samanta, *J. Chem. Phys.* **2018**, *149*, 244102.
- [40] G. Kresse, J. Furthmüller, *Comput. Mater. Sci.* **1996**, *6*, 15–50.
- [41] G. Kresse, J. Furthmüller, *Phys. Rev. B* **1996**, *54*, 11169–11186.
- [42] J. P. Perdew, K. Burke, M. Ernzerhof, *Phys. Rev. Lett.* **1997**, *78*, 1396.
- [43] J. P. Perdew, K. Burke, M. Ernzerhof, *Phys. Rev. Lett.* **1996**, *77*, 3865–3868.
- [44] P. E. Blöchl, *Phys. Rev. B* **1994**, *50*, 17953–17979.
- [45] G. Kresse, D. Joubert, *Phys. Rev. B* **1999**, *59*, 1758–1775.
- [46] M. O. J. Jäger, E. V. Morooka, F. Federici Canova, L. Himanen, A. S. Foster, *NPJ Comput. Mater.* **2018**, *4*, 37.

Manuscript received: February 2, 2022

Accepted manuscript online: March 24, 2022

Version of record online: March 28, 2022